Journal of Solid State Chemistry 258 (2018) 526–535

Contents lists available at ScienceDirect

Journal of Solid State Chemistry

journal homepage: www.elsevier.com/locate/jssc

1D Bi_2S_3 nanorod/2D e-WS_2 nanosheet heterojunction photocatalyst for enhanced photocatalytic activity

S.V. Prabhakar Vattikuti[a,*], Jaesool Shim[a,**], Chan Byon[b]

[a] School of Mechanical Engineering, Yeungnam University, Gyeongsan 712-749, Republic of Korea
[b] School of Mechanical and Nuclear Engineering, Ulsan National Institute of Science and Technology (UNIST), Ulsan 44919, Republic of Korea

ARTICLE INFO

Keywords:
1D
2D
Layered materials
Photocatalysts
Heterojunction
Self-assembled

ABSTRACT

The development of high-activity, long-life, precious-metal-free photocatalysts for redox reactions in photoelectrochemical cells and fuel cells remains challenging. The synthesis of high-activity heterostructured photocatalysts is crucial for efficient energy conversion strategies. Herein, a novel photocatalyst based on 1D Bi_2S_3 nanorods self-assembled on 2D exfoliated tungsten disulfide (e-WS_2) nanosheets has been developed for the degradation of methyl orange (MO) dye in aqueous solution. We demonstrate a novel and facile hydrothermal method for the synthesis of a Bi_2S_3 nanorod/e-WS_2 nanosheet heterostructure. The photocatalytic properties of the heterostructure under visible light were investigated. Enhanced photocatalytic activity was attributed to the presence of strong surface active sites, as well as the specific morphology of the composite. We also observed the fast transfer of electron-hole pairs at the material interface. This work demonstrates a non-noble semiconductor photocatalyst for the degradation of pollutants and evolution of H_2.

1. Introduction

With the recently increased emphasis on the environmental effects of contaminated water from industries such as leather and textiles production, the degradation of pollutants in contaminated water has gained increasing attention from researchers [1–3]. Because it offers high resistance to photocorrosion, TiO_2 is widely considered in the exploration of semiconductor photocatalysts for the degradation of pollutants in aqueous solutions [4,5]. However, TiO_2 is limited in use in photocatalytic applications because it is intrinsically hindered by properties including a wide band gap, low electron mobility, and short hole diffusion length (10–100 nm). Various strategies including doping, co-catalysis, and heterostructure formation have been investigated to address these issues. One of the key research targets for photocatalysts is the development of high-specific-surface-area and high-structural-stability semiconductor heterojunctions. To date, 1D and 2D transition-metal sulfides including FeS_2 [6], Bi_2S_3 [7,8], MoS_2 [9–11], WS_2 [12,13], WSe_2 [14], and $MoSe_2$ [15] have been widely used in photocatalytic applications because they have suitable band gap energies that yield low recombination rates for electron-hole pairs. Compared to 1D metal sulfides, 2D materials exhibit unique characteristics in photocatalytic applications. Bi_2S_3, a visible-light active material with a band gap of 1.25–1.61 eV, has attracted great attention because of its visible-light active photocatalytic performance [16,17]. For example, Sarkar et al. [18] reported that a solvothermally synthesized Bi_2S_3 nanoparticle photocatalyst demonstrated visible irradiation-driven photoactivity towards the degradation of methylene blue, and ascribed this activity to the material's remarkable specific surface area. However, the application of pure Bi_2S_3 in pollutant photodegradation remains limited because the material is relatively low in efficiency and stability, showing rapid recombination of photogenerated electron-hole pairs. The loading of earth-abundant elements as co-catalysts has been an ongoing research subject for the fabrication of low-cost and noble metal-free photocatalysts. Pei et al. [19] reported a heterojunction of Bi_2S_3 and Bi_2MoO_6, which showed enhanced photocatalytic activity with improved charge transfer and separation, as well as diminished charge-carrier recombination. In another study, Wang et al. [20] synthesized a Bi_2MoO_6/Bi_2S_3 photoelectrochemical sensor that has been successfully applied in the selective gallic acid analysis to supervise drug quality. In addition, Bi_2S_3 decorated on Bi_2MoO_6 nanobelts as a platform has exhibited excellent selectivity, reproducibility, and light-harvesting capability. Similarly, Bi_2WO_6/Bi_2S_3 [21–24], $Bi_2S_3/Bi_2Sn_2O_7$ [25], Bi_2S_3/TiO_2 [26], Bi_2S_3/CdS [27], Bi_2S_3/WO_3 [28], Bi_2S_3/Fe_2O_3 [29], $Bi_2S_3/BiPO_4$ [30], Bi_2S_3/g-C_3N_4 [31], Bi_2S_3/Bi_2SiO_5 [32], Bi_2S_3/rGO [33], and various Bi-based [34] heterojunctions have demonstrated excellent photocatalytic activity under visible-light irradiation.

* Correspondence to: School of Mechanical Engineering, Yeungnam University, 214-1 Dae-dong, Gyeongsan-si, Gyeongsangbuk-do 712–749, Republic of Korea.
** Corresponding author.
E-mail addresses: vsvprabu@gmail.com (S.V.P. Vattikuti), jshim@ynu.ac.kr (J. Shim).

https://doi.org/10.1016/j.jssc.2017.11.017
Received 13 September 2017; Received in revised form 7 November 2017; Accepted 10 November 2017
Available online 11 November 2017

2D transition metal dichalcogenides (TMDs) with layered structures have received extensive research attention in the last decade because they have unique structures analogous to graphene and good properties for relevant applications [35,36]. WS_2, an inorganic graphene analog, is a chemically stable layered semiconductor with the band gap of ~1.3 eV, with WS_2 monolayers connected by van der Waals forces. WS_2 is used in various applications including solar cells, gas sensors, Li ion batteries, and the photodegradation of pollutants in aqueous solutions [37]. Thus, WS_2 is considered a suitable candidate for next-generation substitution of noble metals. To fully incorporate the above-mentioned benefits in a single system, the concept of 1D/2D metal sulfide heterojunctions was proposed. To date, little effort has been attempted to grow 1D nanorods on 2D nanosheets, which may be caused by the difficulties in the growth of 1D and 2D nanomaterials in a single synthetic system. For instance, we previously reported that a hydrothermally synthesized CdS/WS_2 hybrid exhibited very high photocatalytic degradation of crystal violet dye under UV and visible-light irradiation [38].

Herein, we report a simple single-step hydrothermally self-assembled Bi_2S_3/exfoliated WS_2 (e-WS_2) nanocomposite for photocatalytic applications. Various approaches have been developed for the synthesis of few-layer e-WS_2, such as mechanical exfoliation, liquid exfoliation, and chemical vapor deposition. Considering the feasibility of operation and the subsequent synthesis of both Bi_2S_3 and e-WS_2, direct sonication in an aqueous solution was employed to obtain few-layer e-WS_2. The ultrasonicated e-WS_2 with more exposed active edges was applied as a co-catalyst for Bi_2S_3 to improve the photocatalytic degradation of methyl orange (MO) dye. The as-synthesized nanocomposite demonstrated excellent photocatalytic efficiency under visible-light irradiation. The electrochemical properties were investigated thoroughly to determine the importance of the heterojunction. This work may facilitate new insights in the selection, design, and construction of noble metal-free photocatalysts for both the photocatalytic degradation of pollutants and sustainable energy generation.

2. Experimental

2.1. Synthesis of few-layer WS_2 and e-WS_2

In a typical synthesis procedure (Scheme 1), 1 mol of WCl_6 and 65 mmol of C_2H_5NS were dissolved in 50 mL of ethanol and 25 mL deionized water under constant stirring. Then, 5 mol/L HCl was used to adjust the pH of the mixed solution to 2–2.5 and the solution was stirred for 1 h at room temperature. Then the above solution was transferred into a 100-mL Teflon-lined stainless steel autoclave, sealed, and maintained at 190 °C for 24 h. After being cooled, the product was obtained by centrifuging, washed repeatedly with deionized water and ethanol three times, and dried in a vacuum oven at 140 °C for 6 h.

To prepare few-layer e-WS_2, a sonication method was employed. Typically, 50 mg of the as-synthesized WS_2 and 100 mL ethanol were added to a beaker, which was submerged in a 200-W ultra-sonication machine for 2 h. The as-obtained homogeneous suspension of e-WS_2 was directly used for the preparation of the Bi_2S_3/e-WS_2heterostructures.

2.2. Synthesis of Bi_2S_3/e-WS_2

We dissolved 2 mmol of Bi $(NO_3)_3{\cdot}5H_2O$ and 3 mmol of $Na_2S{\cdot}9H_2O$ in 25 mL of deionized water under constant stirring. We added 20 mL of HCl to the solution and stirred continuously for 30 min. After stirring, the resultant solution was dissolved into a certain amount of the aforementioned homogeneous suspension of e-WS_2. The nominal weight contents of e-WS_2 in the heterostructures were selected as 1%, 3%, and 5%, denoted as Bi_2S_3/e-WS_2-1%, Bi_2S_3/e-WS_2-3%, and Bi_2S_3/e-WS_2-5%. The obtained mixtures were transferred to a Teflon-lined stainless autoclave and maintained at 190 °C for 24 h. After cooling to room temperature, the precipitates were collected by centrifuging at 8000 rpm and washed with ethanol and water four times. Then, the photocatalysts were dried in a vacuum oven at 120 °C for 8 h.

2.3. Characterization

Powder X-ray diffraction (XRD) patterns of the as-prepared photocatalysts were obtained using a Shimadzu LabX X-ray diffractometer (XRD 6100 model) using Cu Kα radiation (λ= 0.154 nm) at 40 kV and 30 mA. X-ray photoelectron spectroscopy (XPS) analysis was conducted using a Thermo Scientific instrument and K-alpha surface analysis. N_2 adsorption-desorption isotherms were recorded using a Micromeritics ASAP 2420 surface area analyzer at the temperature of liquid N_2. Before gas adsorption, all photocatalysts were degassed for 2 h at 180 °C. To determine the surface morphology and for energy-dispersive X-ray spectroscopy (EDX), images of the powders were taken using scanning electron microscopy (SEM) with a Hitachi S-4800 instrument and transmission electron microscopy (TEM) at an accelerating voltage of 300 kV. High-resolution TEM (HRTEM) studies were performed using a Hitachi H-7000 and a Tecnai G2 F 20 s-twin TEM.

Optical diffuse reflectance spectra (DRS) were recorded at room temperature by UV–visible spectroscopy (Cary 5000 UV–Vis–NIR, spectrophotometer) using the Kubelka–Munk function. The as-prepared powders were placed over a SiO_2 disc during the measurement. Electrochemical impedance spectroscopy (EIS) was measured on an electrochemical workstation (Biologic-Sp-200) with a standard three-electrode system. A 1 M NaOH solution was used as the electrolyte. The photocatalysts prepared in this work were taken as the working electrode, a Pt wire-type electrode as the counter electrode, and Ag/AgCl as the reference electrode. To prepare the working electrode, the as-synthesized 10 mg of pristine Bi_2S_3 or Bi_2S_3/e-WS_2-3% nanocomposite were first dispersed into ethanol (450 μl) and 50 μl Nafion

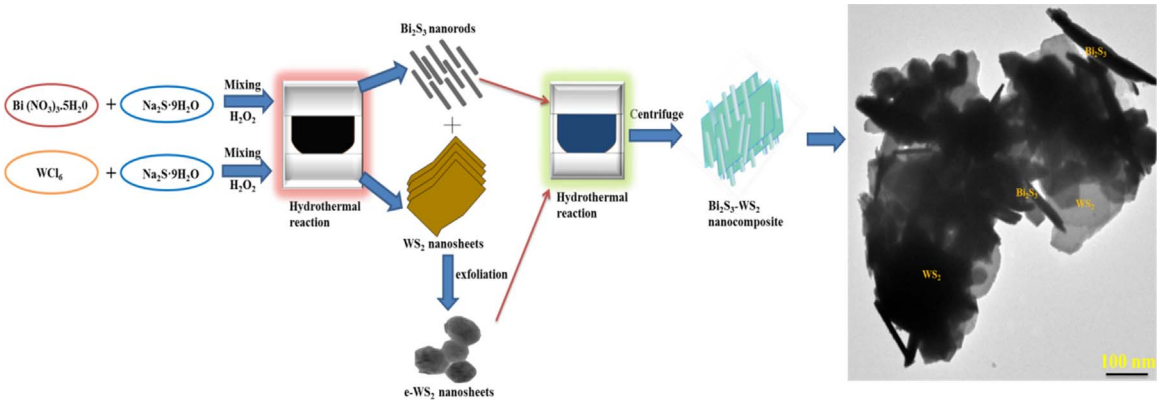

Scheme 1. Schematic illustration of the synthetic procedure of Bi_2S_3 nanorod/e-WS_2 nanosheet heterostructured photocatalyst.

mixtures using soft ultrasonic stirring to obtain a uniform suspension. The solution containing the catalyst (30 μl) was dropped onto the cleaned indium–tin oxide (ITO) conductor glass substrate, which was then dried in an oven at 90 °C for 4 h. Experimental studies for EIS were performed using a potentiostat with a sinusoidal perturbation voltage of 2 mV rms in the frequency range of 0.01 Hz to 1 MHz.

2.4. Photocatalytic test

Typically, the photocatalytic activity of the as-prepared nanocomposite was tested at the natural pH of a MO organic dye solution (4 ppm in concentration). The test was performed under visible-light irradiation with a Xenon lamp (λ > 400 nm). In a typical run, a mixture comprising 20 mg of various photocatalysts was suspended in 100 mL of MO aqueous solution and stirred for 60 min in order to achieve an adsorption-desorption equilibrium mixture. During light irradiation, 5 mL of the reaction mixture was sampled at 15-min intervals with a syringe. The collected samples were examined with a UV–Vis–NIR Cary 500 spectrophotometer. The photocatalysts were then separated from the degraded solution by centrifuging (5000 rpm), washed with ethanol to fully take away the residual dye moieties then again washed with water and reused for consequent runs.

3. Results and discussion

3.1. Structure, composition, and morphological features

Fig. 1 shows the XRD patterns of the pristine Bi_2S_3 nanorods, e-WS_2nanosheets, and Bi_2S_3 nanorod/e-WS_2 nanosheet heterostructures. For the pristine Bi_2S_3 nanorods, 18 distinctive peaks at 2θ = 11.14°, 15.67°, 17.59°, 23.71°, 24.94°, 28.65°, 31.82°, 33.93°, 35.61°, 39.93°, 42.7°, 46.5°, 48.29°, 52.61°, 54.74°, 62.61°, 68.54°, and 78.78° are well matched with the standard pattern of orthorhombic Bi_2S_3 (JCPDS-89–8964) [39]. For the e-WS_2 nanosheets, diffraction peaks at 14.32°, 28.87°, 32.57°, 33.57°, 35.9°, 39.5°, 43.91°, 49.71°, 58.46°, 59.81°, and 66.51° are observed. These peaks are indexed to the (002), (004), (100), (101), (102), (103), (006), (105), (110), (008), and (114)

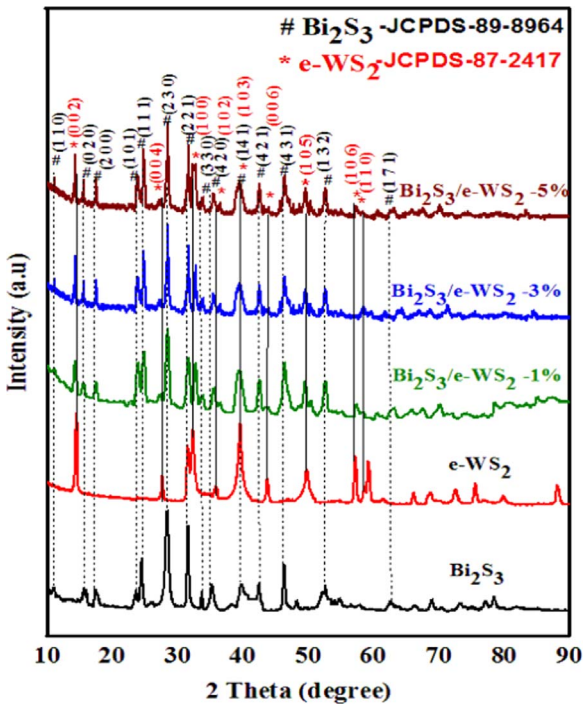

Fig. 1. XRD pattern of as-prepared Bi_2S_3 nanorods, e-WS_2 nanosheets, and various Bi_2S_3 nanorod/e-WS_2 nanosheet heterostrucuted photocatalysts.

planes of hexagonal WS_2 (JCPDS card No. 87–2417) [38,40]. Whereas, for all hybrid photocatalysts, all the peaks are well matched with either Bi_2S_3 or WS_2; no impurity peaks are found.

Fig. 2 presents SEM images of the as prepared WS_2 nanosheets and e-WS_2 nanosheets (Fig. 2a, b), which are stacked on each other. The pristine Bi_2S_3 nanorods of a few nanometers in length can be seen in Fig. 2c. The surfaces of the Bi_2S_3 nanorods are randomly covered with a few layers of dense e-WS_2 nanosheets (Fig. 2d-f). Thus, heterostructures are formed, which can facilitate fast carrier transfer at the material interface. Moreover, elemental mapping of the as-prepared WS_2 nanosheets and Bi_2S_3 nanorod/e-WS_2 nanosheet heterostructure (Fig. 2g, h) confirms the formation of a two-phase structure; Bi, W, and S elements are found with no impurities indicated in the EDX spectra. No impurity peaks are observed, reflecting the purity of all samples. In addition, SEM image and EDX elemental mapping (Fig. 2i-l) verifies the purity of the heterostructure nanocomposite of the Bi_2S_3/e-WS_2-3% photocatalyst.

The HRTEM image in Fig. 3a, b presents the as-synthesized WS_2 nanosheets. It can be seen that layered WS_2 nanosheets are agglomerated together, blocking active sites and thus causing low photoactivity. Therefore, we attempted to exfoliate these nanosheets and use them as a co-catalyst in the preparation of the heterostructure to improve the photocatalytic performance. Fig. 3b and c show the exfoliated WS_2 (e-WS_2) nanosheets achieved by simple sonication; their morphologies match well with the above SEM results (Fig. 2a). The dotted selected-area electron diffraction (SAED) pattern of e-WS_2 nanosheets is shown in Fig. 3d. After adding 1D Bi_2S_3 nanorods to the e-WS_2 nanosheets, the Bi_2S_3 nanorod/e-WS_2 nanosheet heterostructure retains 1D/2D morphologies. An ultrathin layer of e-WS_2 nanosheets is observed on the surfaces of the randomly distributed 1D Bi_2S_3 nanorods, as shown in Fig. 4a-c. The high-resolution TEM image of the Bi_2S_3/e-WS_2-3% heterostructure is shown in Fig. 4d, reveals the interplanar spacings of 0.36 and 0.315 nm, which corresponds to the (130) crystal plane of orthorhombic Bi_2S_3 and the (102) crystal plane of hexagonal WS_2, respectively. The SAED pattern of the Bi_2S_3 /e-WS_2- 3%heterostructure is shown in the inset in Fig. 4d, having bright superimposed patterns with interlinked line patterns and white spots organized in a linear manner. This further demonstrates that the material is a single composite, indicating the formation of a heterostructure.

XPS measurements were used to confirm the valence and state of each element in the Bi_2S_3 nanorod/e-WS_2 nanosheet heterostructure. The XPS survey spectra of Bi_2S_3 /e-WS_2-3% photocatalyst are shown in Fig. 5a. From Fig. 5b, it is observed that the two broadened peaks and two small peaks at 158.54, 163.92, 161.64, and 162.88 eV correspond to the Bi $4f_{7/2}$, Bi $4f_{5/2}$, S $2p_{3/2}$, and S $2p_{5/2}$ components in Bi_2S_3, respectively [41], further verifying the formation of Bi_2S_3. From Fig. 5c, the W 4*f* spectrum can be deconvoluted into two major peaks at 32.48 and 34.74 eV, assigned to the W $4f_{7/2}$ and W $4f_{5/2}$ species in WS_2; a low-intensity peak from W$5p_{5/2}$ is observed at 37.5 eV [42]. From Fig. 5d, two peaks at 161.64 and 162.88 eV are assigned to S $2p_{3/2}$ and S $2p_{5/2}$, indicating the presence of bridging S_2^{2-} or apical S^{2-}, which are the active sites in photocatalytic reactions.

The UV–vis DRS spectra of pristine Bi_2S_3, e-WS_2, and Bi_2S_3/e-WS_2-3% photocatalysts are shown in Fig. 6. All the absorption peaks of the photocatalysts are located in the visible region. However, upon the deposition of thin e-WS_2 nanosheets on the surface of the Bi_2S_3 nanorods, a remarkable red shift was observed in absorption of the heterostructure, ascribed to the surface morphological features of the 1D/2D heterostructure. The band gap energies of the Bi_2S_3 nanorods, e-WS_2, and Bi_2S_3/e-WS_2-3% photocatalysts are 1.32, 1.51, and 1.47 eV, respectively.

3.2. Photocatalytic activity

Recent studies have detailed the uses of layered nanomaterials as co-catalysts, including MoS_2 [43], WS_2 [44], and g-C_3N_4 [45], and

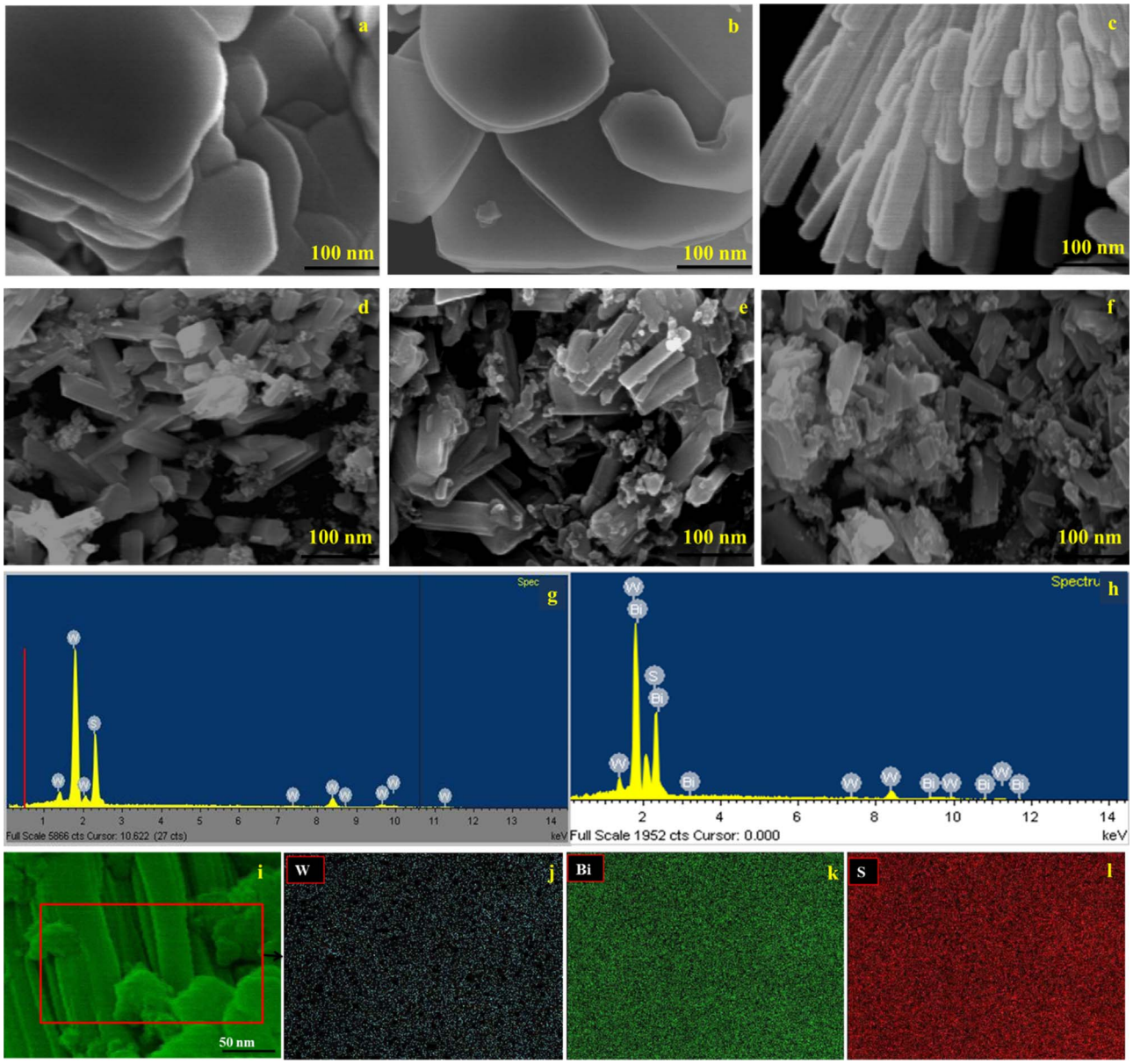

Fig. 2. SEM images of (a) as-prepared WS_2, (b) e-WS_2, (c) as-prepared Bi_2S_3, (d) Bi_2S_3/e-WS_2-1%, (e) Bi_2S_3/e-WS_2-3%, and (f) Bi_2S_3/e-WS_2-5% photocatalysts, EDX spectrum of (g) as-prepared WS_2, and (h) Bi_2S_3 /e-WS_2-3% photocatalyst, (e) SEM image and SEM elemental mapping (j-l) of Bi_2S_3 /e-WS_2-3% photocatalyst.

discussed their photocatalytic properties. MoS_2 as a co-catalyst can improve the photosensitization of Bi_2S_3 to 2.02 times higher than that of pristine Bi_2S_3 [46]. Based on these previous reports, we found that the photocatalytic activity of Bi_2S_3 is enhanced after combination with e-WS_2 nanosheets, which act as co-catalysts. The catalytic activity of the Bi_2S_3/e-WS_2 heterostructured photocatalyst toward the decomposition of MO dye was studied. Fig. 7a shows the UV–visible spectra of the photocatalytic decomposition of MO over the Bi_2S_3/e-WS_2-3% photocatalyst. Fig. 7a shows two characteristic peaks at 464 nm and 273 nm, corresponding to the monomer and dimer of MO. In order to completely understand the photocatalytic performance; three different sets of experiments were performed as follows: (i) MO pollutant, without the photocatalyst, was irradiated with visible light; (ii) MO pollutant was reacted with the photocatalysts without visible light irradiation; and (iii) MO pollutant and photocatalysts were irradiated with visible light. Fig. 7b shows the photocatalytic performance of the Bi_2S_3, e-WS_2, Bi_2S_3/e-WS_2-1%, Bi_2S_3/e-WS_2-3%, and Bi_2S_3/e-WS_2-5% photocatalysts, investigated by the degradation of aqueous MO solution under visible-light irradiation. Initially, the photocatalytic experiments were performed without and with photocatalysts under dark condition for 15 min. The results from these experiments revealed that the photocatalysts by themselves showed either no catalytic activity or absorption by MO in the dark with negligible adsorption. After 90 min of irradiation in the presence of the Bi_2S_3/e-WS_2-3% photocatalyst, 88.4% MO dye is decomposed from the aqueous solution. It can be clearly seen that the Bi_2S_3 nanorod/e-WS_2 nanosheet heterostructures show improved photodegradation efficiency under visible-light irradiation. The as-synthesized WS_2shows a lower MO photodegradation rate under visible-light irradiation because of the agglomeration of nanosheets compared to the rates of pristine Bi_2S_3 nanorods and e-WS_2 nanosheets, in accord with past studies [47]. The photodegradation rate of the e-WS_2 nanosheets reaches 63.1% after 90 min of visible light irradiation. The photodegradation rate of MO with the Bi_2S_3 nanorod/e-WS_2 nanosheet heterostructures reaches the maximum of 88.4% for 90 min irradiation over the Bi_2S_3/e-WS_2-3% photocatalyst, better than that of the e-WS_2 nanosheets (74.3%), pristine Bi_2S_3 nanorods (62.1%), and as-synthesized WS_2 (51.3%). Therefore, the Bi_2S_3 nanorod/e-WS_2 nanosheet heterostructures show more prominent photocatalytic activ-

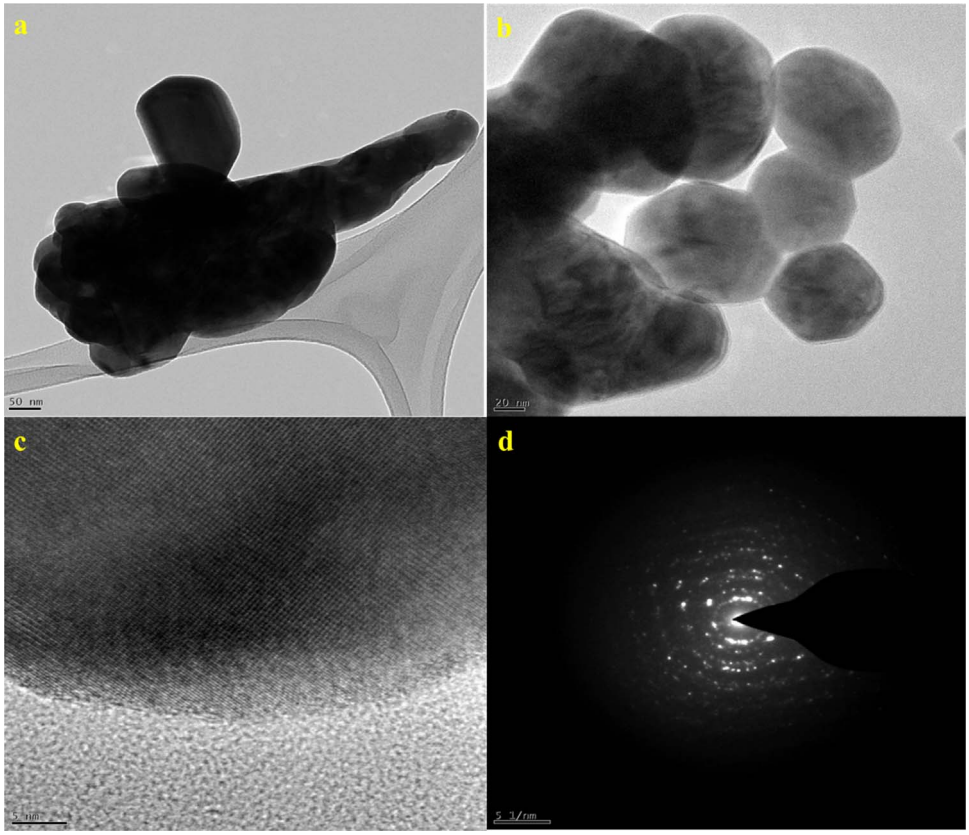

Fig. 3. (a) HRTEM image of as-prepared WS_2, (b, c) HRTEM images, and (d) SAED pattern of e-WS_2.

ity than the Bi_2S_3 nanorods or e-WS_2 nanosheets alone. The kinetic linear simulations of MO photocatalytic degradation over the different photocatalysts are shown in Fig. 7c.

It was observed that, as the amounts of e-WS_2 nanosheets increased, the photocatalytic activities of Bi_2S_3 nanorod/e-WS_2 nanosheet heterostructures were initially increased, achieved the maximum value at 3 wt% loading of e-WS_2, and were decreased with the further loading of e-WS_2. This can be explained as follows: With 1 wt% loading of e-WS_2, the photocatalytic properties of the e-WS_2 nanosheets are enhanced by the nanosheet compositing with Bi_2S_3 nanorods, which are active under visible-light irradiation with good light absorption capability. When the loading of e-WS_2 is increased to 3 wt%, the photocatalytic properties of the Bi_2S_3 nanorod/e-WS_2 nanosheet heterostructures are improved with the increased e-WS_2 nanosheet concentration. However, with the maximum loading of 5 wt % e-WS_2, the photocatalytic properties of the Bi_2S_3 nanorod/e-WS_2 nanosheet heterostructure are decreased because the excessive amount of e-WS_2 covers the active sites of the Bi_2S_3 nanorods, and promotes the aggregation of e-WS_2 nanosheets, thereby hindering electron transfer at the heterostructure interface. These aspects inhibit the photocatalytic performance.

Comparing the Bi_2S_3/e-WS_2 hybrid photocatalysts in terms of the loading of e-WS_2 contents, we can observe the dependence of photocatalytic degradation on the e-WS_2 content. Noticeably, the concentration of e-WS_2 is proportional to the photodegradation activity of the hybrid photocatalyst. However, the photodegradation activity of Bi_2S_3/e-WS_2-5% is less than that of Bi_2S_3/e-WS_2-3%. The Langmuir–Hinshelwood (L–H) kinetics model reveals this difference (Fig. 7c), and the photocatalytic degradation process of MO can be stated as the following pseudo-first order kinetics equation [48]:

$$\mathrm{In}\frac{Co}{C} = \mathrm{k}_{app}t \quad (1)$$

Where C is the MO concentration at time t, C_0 is the initial concentration of the MO solution, and K_{app} is the apparent pseudo-first-order rate constant (min^{-1}). Based on the measured photocatalytic activities, we assert that the content of e-WS_2strongly influences the photocatalytic efficiency of the Bi_2S_3/e-WS_2 hybrid. In particular, the excessive addition of e-WS_2 nanosheets promotes the recombination of photo-induced carriers of electron-hole pairs, rather than forming an electron conduction path [19,46]. This may explain the reduced photodegradation property of Bi_2S_3/e-WS_2-5% and is consistent with results reported previously in the literature [47].

To investigate the photocatalytic stability and reusability of the photocatalysts, repeated cyclic tests were performed for three cycles are shown in Fig. 7d. After each cycle, the photocatalyst was collected by centrifuging, filtered, dried thoroughly, and then reused with a fresh MO aqueous solution to retest the photocatalytic activity. After three cycles, the Bi_2S_3/e-WS_2-3% photocatalyst maintains good catalytic activity with negligible deviation and good stability under visible-light irradiation.

To better understand the charge separation and transport processes of the Bi_2S_3 nanorod/e-WS_2 nanosheet heterostructures, the photocatalysts were investigated using EIS measurements and transient photocurrent studies. The impedance plots of all photocatalysts are shown in Fig. 8a, with the radius of each arc relating to the charge-transfer process. Smaller arc radii in the EIS spectra of the hybrid photocatalysts indicate lower electron-transfer resistance at the photoelectrodes, because of both more effective charge separation and faster interfacial charge transport. The arc radii of the pristine Bi_2S_3 and e-WS_2 photocatalysts are the largest, whereas those of the hybrid photocatalysts are the smallest. Remarkably, the Bi_2S_3/e-WS_2-3% photocatalyst exhibits a very low electron transfer resistance. The photocurrent studies were performed under repeated on-off cycles using the as-prepared Bi_2S_3 and Bi_2S_3/e-WS_2-3% photocatalyst as photo anode, Pt wire and Ag/AgCl (SCE) used as a cathode and

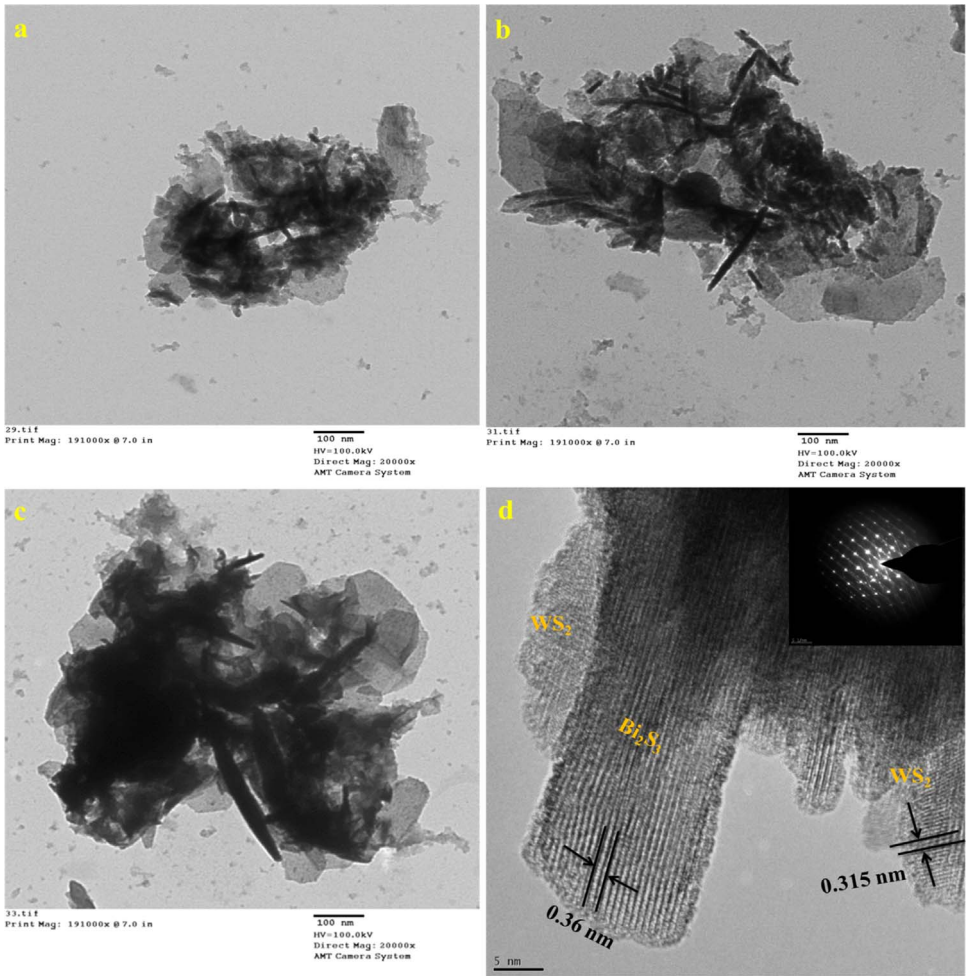

Fig. 4. TEM images (a) Bi_2S_3/e-WS_2-1%, (b) Bi_2S_3/e-WS_2-3%, and (c) Bi_2S_3/e-WS_2-5% photocatalysts, and (d) HRTEM image (inset: SAED pattern) of Bi_2S_3 /e-WS_2-3% photocatalyst.

reference electrode, respectively. Fig. 8b showed the current time (I–t) characteristics curve of as prepared Bi_2S_3 and Bi_2S_3/e-WS_2-3% photocatalyst electrodes. Both electrodes demonstrated a distinct visible light photocurrent response during the on/off illumination cycles represents quick photoinduced charge transfer from electrode materials. Among these, Bi_2S_3/e-WS_2-3% electrode exhibited higher photocurrent response compared to the as-prepared Bi_2S_3 electrode. Obviously, the enhanced photocurrent response is partly due to the increased light absorption as well as reduced charge recombination effect may be another reason for the improved photocurrent density with Bi_2S_3/e-WS_2-3% electrode. The as-synthesized heterostructure has rapid charge-separation features and more effective carrier transfer compared to those of pristine 1D Bi_2S_3 nanorods or e-WS_2 nanosheets. As a result, it is concluded that the formation of a heterojunction between the binary materials is beneficial for efficient charge separation, fast electron transport, and light harvesting.

The enhanced photocatalytic properties of the Bi_2S_3 nanorod/e-WS_2 nanosheet heterostructures under visible-light irradiation may be ascribed to several features. Based on the DRS results, the Bi_2S_3 nanorod/e-WS_2 nanosheet heterostructures have narrow band gaps that provide improved visible light absorption, and can therefore, absorb more visible light than the pristine Bi_2S_3 and e-WS_2 nanosheets; thus, the photoactivity is improved. The heterostructures also have larger specific surface areas, which facilitate faster electron transfer because there are more active sites. The high specific surface area of the 1D/2D heterostructure facilitates enhanced absorption of incident light by the increased active sites, which enhances the adsorption and photodegradation of MO dye in aqueous solutions. In addition, the high surface area improves the absorption of oxygen on the heterojunction surfaces; this absorbed oxygen can react with photogenerated electrons. The Bi_2S_3 nanorod/e-WS_2 nanosheet heterostructures have higher Brunauer–Emmett–Teller (BET) surface areas of 68.25 $m^2 g^{-1}$ (Fig. 9) than pristine Bi_2S_3 nanorods have (24.67 $m^2 g^{-1}$) [48]. Strong contacts at the heterojunction interface effectively diminish the recombination of photoelectrons and holes, which reflects longer life spans for both charge species. The morphological features of 1D/2D heterostructures can achieve the efficient separation of electrons and holes and facilitate the migration of photoinduced carriers. Finally, the 1D/2D porous structure can improve the photon utilization capability, thereby enhancing the interaction between dye molecules and photocatalyst.

Based on the above results and discussion, it is clear that the generation and separation of electron-hole pairs is efficiently enhanced by the photocatalytic properties of the Bi_2S_3 nanorod/e-WS_2 nanosheet heterostructure under visible-light irradiation. The photocatalytic mechanism of the heterostructure is shown in Scheme 2. The calculated conduction band (CB) edge potentials (E_{CB}) of the pristine Bi_2S_3 and e-$WS_2$are approximately −0.55 and 0.27 eV, respectively; the valence band (VB) edge potentials (E_{VB}) are approximately 0.77 and 1.79 eV, respectively. From the Scheme 2 under visible-light irradiation, both Bi_2S_3 and e-WS_2 can excite the photoinduced electrons to the CB and create holes in the VB. Because the E_{CB} of Bi_2S_3 (−0.55 eV) is lower than that of e-WS_2 (0.27 eV), electrons in the CB of Bi_2S_3 can be transferred to the CB of e-WS_2 by the heterojunction interface, thereby separating the charge carriers. In addition, the E_{VB} of Bi_2S_3 (1.79 eV) is higher than that of e-WS_2 (0.77 eV); therefore, holes in the VB of e-

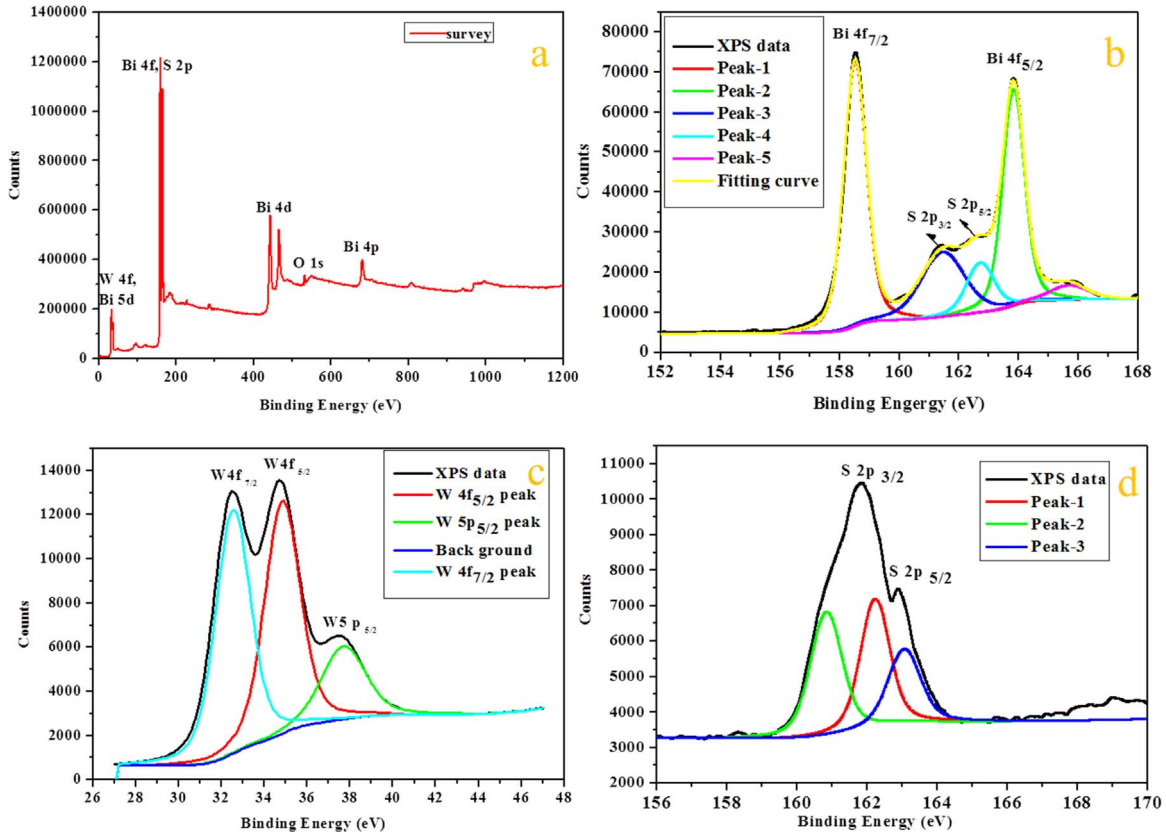

Fig. 5. High resolution X-ray photoelectron spectra (a) survey, (b) Bi, (c) W and (d) S elements of Bi_2S_3 /e-WS_2-3% photocatalyst.

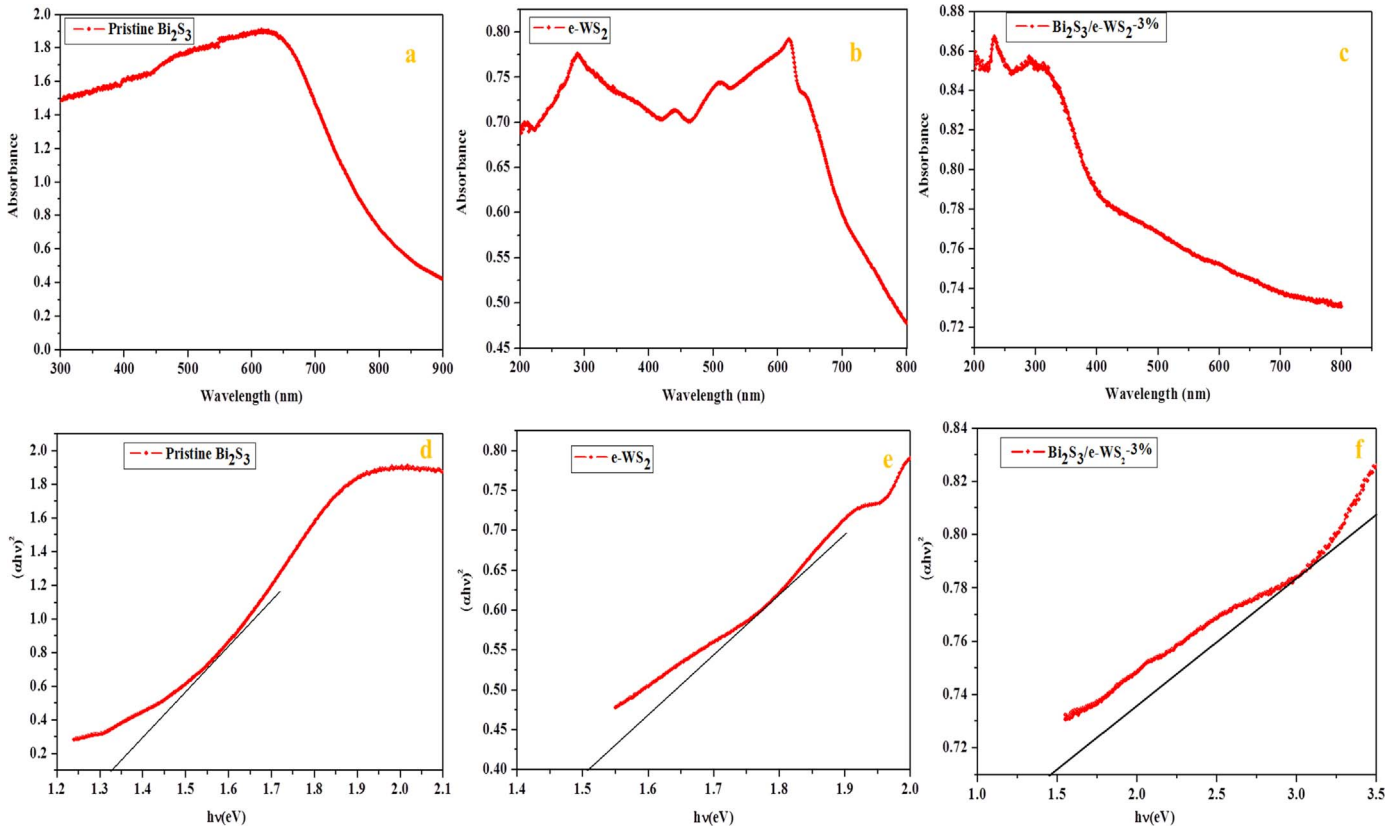

Fig. 6. UV–vis spectra (a-c) and (d-f) Tauc plots of as-prepared Bi_2S_3 nanorods, e-WS_2 nanosheets and Bi_2S_3/e-WS_2-3% photocatalyst.

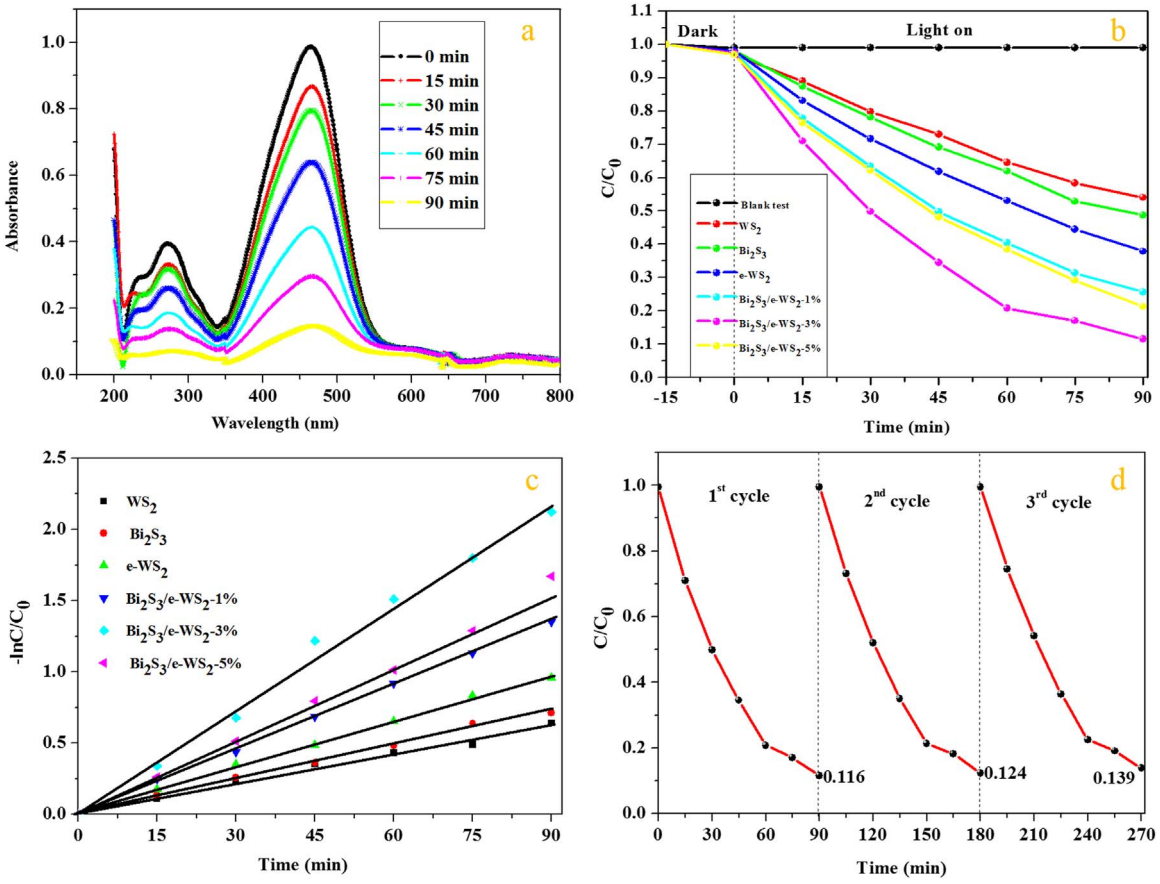

Fig. 7. (a) Time-dependent visible light absorbance spectra of the MO solution along with Bi_2S_3/e-WS_2-3% photocatalyst taken at different times, (b) photocatalytic degradation activities and (c) the kinetic plot of photocatalytic degradation with various photocatalysts under visible light irradiation, and (d) recycling and reusability performance test of Bi_2S_3/e-WS_2-3% photocatalyst.

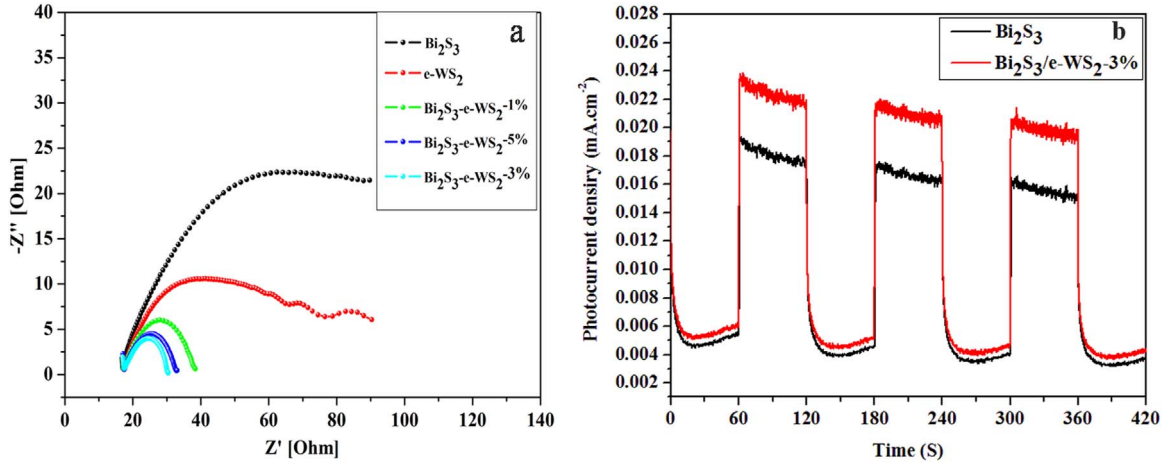

Fig. 8. (a) Electrochemical impedance spectra of as-prepared Bi_2S_3 nanorods, e-WS_2 nanosheets, and various Bi_2S_3 nanorod/e-WS_2 nanosheet heterostrucuted photocatalysts, and (b) transient photocurrent studies of as prepared Bi_2S_3 and Bi_2S_3/e-WS_2-3% photocatalyst.

WS_2 can migrate to the VB of Bi_2S_3, hindering photogenerated electron-hole recombination in Bi_2S_3 and e-WS_2. Further, the photo-induced electrons reacts with the O_2 molecules absorbed on the Bi_2S_3 nanorod/e-WS_2 nanosheet heterostructure surface to form O_2^-. Meanwhile, the photoinduced holes can react with the H_2O/OH^- to form OH• radicals [49]. Therefore, with the strong oxidizing agents of O_2^- and OH•, the Bi_2S_3 nanorod/e-WS_2 nanosheet heterostructure can oxidize organisms and organic pollutants into CO_2 and H_2O molecules, as following:

$$Bi_2S_3/e\text{-}WS_2 + h\upsilon \rightarrow Bi_2S_3/e\text{-}WS_2\ (h^+ + e^-) \quad (2)$$

$$Bi_2S_3/e\text{-}WS_2\ (h^+ + e^-) \rightarrow e\text{-}WS_2\ (e^-)/Bi_2S_3\ (h^+) \quad (3)$$

$$e\text{-}WS_2\ (e^-) + O_2 \rightarrow e\text{-}WS_2 + \cdot O_2^- \quad (4)$$

$$Bi_2S_3\ (h^+) + H_2O \rightarrow OH\cdot + H^+ \quad (5)$$

$$O_2^- + H_2O \rightarrow HO_2\cdot + OH^- \quad (6)$$

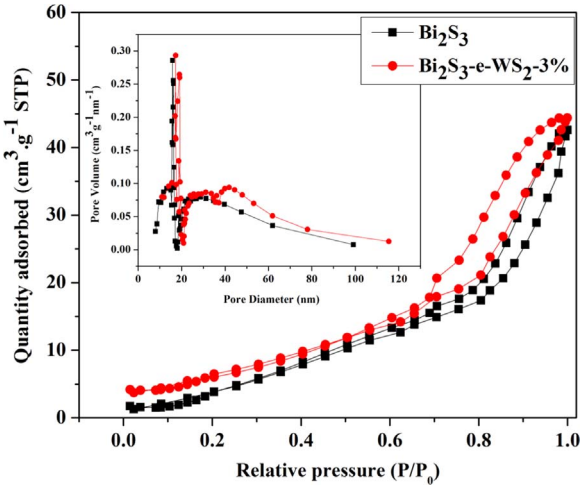

Fig. 9. N_2 adsorption/desorption isotherm, inset: pore size distribution of as-prepared Bi_2S_3 nanorods and Bi_2S_3/e-WS_2-3% photocatalyst.

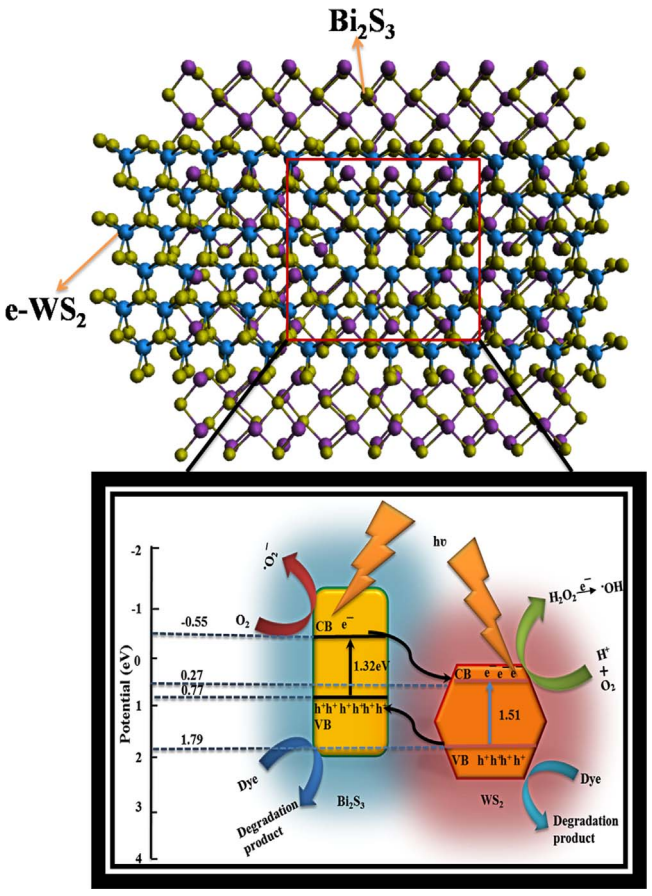

Scheme 2. Schematic illustrations for the mechanism of photoinduced charge carrier transfers in Bi_2S_3 nanorod/e-WS_2 nanosheet heterostructured photocatalyst under visible light irradiation.

$$HO_2\cdot + H_2O \rightarrow H_2O_2 + OH\cdot \quad (7)$$

$$H_2O_2 \rightarrow 2OH\cdot \quad (8)$$

$$OH\cdot + \text{organism} \rightarrow CO_2 + H_2O \quad (9)$$

Thus, the improvement of photocatalytic activity under visible-light irradiation may be ascribed to the coupling effect of Bi_2S_3 and e-WS_2. Coupling facilitates efficient charge-separation by the oriented transfer of electrons and holes from the semiconductor to another material, which provides the Bi_2S_3 nanorod/e-WS_2 nanosheet heterostructures with remarkable photocatalytic activities as visible-light-driven photocatalysts.

4. Conclusions

In summary, we have rationally designed and developed a novel 1D Bi_2S_3 nanorod/2D e-WS_2 nanosheet heterojunction as a photocatalyst for the photodegradation of MO. A dense layer of e-WS_2 ultrathin nanosheets decorated on the surfaces of the Bi_2S_3 nanorods. Because of this heterojunction nanostructure, the photocatalyst exhibits the enhanced photodegradation of MO at a rate 1.42 and 1.19 times higher than those achieved by pristine Bi_2S_3 and e-WS_2, respectively. EIS measurement results show that fast electron-hole separation and excellent charge transfer contribute to the improved photocatalytic activity. The improved performance can be attributed to (i) the 1D/2D porous structure, (ii) the large specific surface area, (iii) well-matched band energies, (iv) enhanced charge transfer efficiency, and (v) diminished photoelectron–hole recombination. We believe that our findings demonstrate a promising method to design complex 1D/2D heterojunctions for application in hydrogen evolution and photoelectrochemical sensing applications.

Acknowledgments

This research was supported by the National Research Foundation of Korea (NRF) and funded by the Ministry of Science, ICT, and Future Planning (2017R1A2B1004860). This work was supported by the National Research Foundation of Korea (NRF) grant funded by the Korea government (No. NRF-2015R1A2A2A01003741) and (No. NRF-2017R1A4A1015581). This research was supported by the 2017 Research Fund (1.170013.01) of UNIST (Ulsan National Institute of Science & Technology).

References

[1] A. Fujishima, K. Honda, Nature 238 (1972) 37–38.
[2] U.M. Sh, M. Khan, W.B.I. Al-Shahry Jr, Science 297 (5590) (2002) 2243–2245.
[3] B. Luo, G. Liu, L. Wang, Nanoscale 8 (2016) 6904–6920.
[4] A.A. Ismail, D.W. Bahnemann, J. Mater. Chem. 21 (2011) 11686–11707.
[5] Y. Qu, X.F. Duan, Chem. Soc. Rev. 42 (2013) 2568–2580.
[6] M. Barawi, I.J. Ferrer, E. Flores, S. Yoda, J.R. Ares, C. Sánchez, J. Phys. Chem. C 120 (18) (2016) 9547–9552.
[7] S.V.P. Vattikuti, J. Shim, Ch Byon, J. Mater. Sci: Mater. Electron 28 (2017) 14282–14292.
[8] T. Wu, X. Zhou, H. Zhang, X. Zhong, Nano Res. 3 (2010) 379–386.
[9] E. Parzinger, B. Miller, B. Blaschke, J.A. Garrido, J.W. Ager, A. Holleitner, U. Wurstbauer, ACS Nano 9 (11) (2015) 11302–11309.
[10] T.R. Thurston, J.P. Wilcoxon, J. Phys. Chem. B 103 (1) (1999) 11–17.
[11] S.V.P. Vattikuti, Ch Byon, Ch.V. Reddy, Superlattic Microstruct. 85 (2015) 124–132.
[12] C.Y. Luo, W.Q. Huang, W. Hu, P. Peng, G. Huang, Dalton Trans. 45 (2016) 13383–13391.
[13] S.V.P. Vattikuti, Ch Byon, Sci. Adv. Mater. 7 (12) (2015) 2639–2645.
[14] X. Yu, M.S. Prévot, N. Guijarro, K. Sivula, Nat. Commun. 6 (2015) 7596.
[15] H. Chu, W. Lei, X. Liu, J. Qu, J. Li, G.Z. Lengyuan, N.L. Pan, J. Mater. Sci. Mater. Electron. 27 (5) (2016) 5483–5489.
[16] H. Zhang, J. Huang, Xi Zhou, X. Zhong, Inorg. Chem. 50 (16) (2011) 7729–7734.
[17] P. Han, A. Mihi, J. borrull, J. Pallarés, L.F. Marsal, J. Phys. Chem. C 119 (19) (2015) 10693–10699.
[18] A. Sarkar, A. Ghosh, N. Saha, D.N. Srivastava, P. Paul, B. Adhikary, J. Colloid Interface Sci. 483 (2016) 49–59.
[19] Y. Pei, X. Li, H. Chu, Y. Ge, P. Dong, R. Baines, L. Pei, M. Ye, J. Shen, Talanta 165 (2017) 44–51.
[20] L. Wang, Z. Liu, D. Wang, S. Ni, D. Han, W. Wang, Li Niu, Biosens. Bioelectron. 94 (2017) 107–114.
[21] L. Yan, Y. Wang, H. Shen, Y. Zhang, J. Li, D. Wang, Appl. Surf. Sci. 393 (2017) 496–503.
[22] X. Li, Y. Li, J. Shenn, M. Ye, Ceram. Int. 42 (2016) 3154–3162.
[23] A. Rauf, Md.S.S. Shah, G.H. Choi, U.B. Humayoun, D.H. Yoon, J.W. Bae, J. Park, W. Kim, P.J. Yoo, ACS Sustain. Chem. Eng. 3 (2015) 2847–2855.
[24] Qi Zhanga, Zan Daia, Gang Chenga, YunLing Liub, Rong Chen, Ceram. Int. 43 (2017) 11296–11304.

[25] W. Xu, J. Fang, Y. Chen, Sh Lu, G. Zhou, X. Zhu, Z. Fang, Mater. Chem. Phys. 154 (2015) 30–37.
[26] S. Kumar, Sh Sharma, S. Sood, A. Umar, S.K. Kansal, Ceram. Int. 2 (2016) 17551–17557.
[27] L. Hao, G. Chen, Y. Yu, Y. Zhou, Zh Han, Y. Liu, Int. J. Hydrog. Energy 39 (2014) 14479–14486.
[28] J. Rong, T. Zhang, F. Qiu, X. Rong, X. Zhu, X. Zhang, J. Alloy. Compd. 685 (2016) 812–819.
[29] A. Helal, F.A. Harraz, A.A. Ismail, T.M. Samic, I.A. Ibrahim, Appl. Catal. B: Environ. 213 (2017) 18–27.
[30] M. Lu, G. Yuan, Z. Wang, Y. Wang, J. Guo, Nanoscale Res. Lett. 10 (2015) 385–391.
[31] X. Rong, F. Qiu, J. Yan, H. Zhao, X. Zhu, D. Yang, RSC Adv. 5 (2015) 24944–24952.
[32] X. Liu, W. Wang, Y. Liu, B. Huang, Y. Dai, X. Qin, X. Zhang, RSC Adv. 5 (2015) 55957–55963.
[33] Y. Chen, G. Tian, G. Mao, R. Li, Y. Xiao, T. Han, Appl. Surf. Sci. 378 (2016) 231–238.
[34] R. He, S. Cao, P. Zhou, J. Yu, Chin. J. Catal. 35 (2014) 989–1007.
[35] W. Choi, N. Choudhary, G.H. Han, J. Park, D. Akinwande, Y.H. Lee, Mater. Today 20 (3) (2017) 116–130.
[36] Q. Lu, Y. Yu, Q. Ma, B. Chen, H. Zhang, Adv. Mater. 28 (10) (2016) 1917–1933.
[37] K.Y. Ko, J. Song, Y. Kim, T. Choi, S. Shin, Ch.W. Lee, K. Lee, J. Koo, H. Lee, J. Kim, T. Lee, J. Park, H. Kim, ACS Nano 10 (2016) 9287–9296.
[38] S.V.P. Vattikuti, I. Ngo, C. Byon, Solid State Sci. 61 (2016) 121–130.
[39] S.V.P. Vattikuti, C. Byon, Superlattice. Microstruct. 100 (2016) 514–525.
[40] R. Wei, X. Tian, H. Zhang, Z. Hu, X. He, Z. Chen, Q. Chen, J. Qiu, J. Alloy. Compd. 684 (2016) 224–229.
[41] C. Chen, X. Qiu, S. Ji, C. Jia, C. Ye, Cryst. Eng. Commun. 15 (2013) 7644–7648.
[42] S.V.P. Vattikuti, C. Byon, V. Chitturi, Superlattice Microstruct. 100 (2016) 514–525.
[43] L. Wei, Y. Chen, Y. Lin, H. Wu, R. yuan, Z. Li, Appl. Catal. B: Environ. 144 (2014) 521–527.
[44] X. Zong, J. Han, G. Ma, H. Yan, G. Wu, C. Li, J. Phys. Chem. C 115 (24) (2011) 12202–12208.
[45] Y. Zheng, Y. Jiao, Y. Zhu, Q. Cai, A. Vasileff, L.H. Li, Y. Han, Y. Chen, S. Qiao, J. Am. Chem. Soc. 139 (9) (2017) 3336–3339.
[46] B. Weng, X. Zhang, N. Zhang, Z. Tang, Y. Xu, Langmuir 31 (14) (2015) 4314–4322.
[47] C.H. Wu, H.W. Chang, J.M. Chern, J. Hazard. Mater. 137 (2006) 336–343.
[48] H.W. Ma, J.F. Shen, M. Shi, X. Lu, Z.Q. Li, Y. Long, N. Li, M.X. Ye, Appl. Catal. B: Environ. 121–122 (2012) 198–205.
[49] J. Jin, T. He, Appl. Surf. Sci. 394 (2017) 364–370.